ORIGINAL ARTICLE

Journal Section

Optical coherence tomography for *in vivo* longitudinal monitoring of artificial dermal scaffold

Ziye Chen[1*] | **Qiong Cheng[2*]** | **Lingyun Wang[1]** | **Yunfeng Mo[1]** | **Ke Li PHD[2]** | **Jianhua Mo PHD[1]**

[1]School of Electronics and Information Engineering, Soochow University, Suzhou, China

[2]Department of Burn and Plastic Surgery, the First Affiliated Hospital of Soochow University, Suzhou, China

Correspondence

Jianhua Mo PhD, School of Electronics and Information Engineering, Soochow University, Suzhou, No.333 Ganjiang East Road, 215006, China
Email: joshuamo@gmail.com

Objectives. Artificial dermal scaffold (ADS) has undergone a rapid development and been increasingly used for treating skin wound in clinic due to its good biocompatibility, controllable degradation, and low risk of disease infection. To obtain a good treatment efficacy, ADS needs to be monitored longitudinally during the treatment process. For example, the fit of the scaffold with the underlying natural tissue and the degradation rate are two key properties to be inspected. However, to date, there are no effective, real-time and non-invasive techniques to meet the requirement of the scaffold monitoring above.

Materials and Methods. In this study, we propose to use optical coherence tomography (OCT) to monitor the ADS *in vivo* through three-dimensional imaging. A swept source OCT system with a handheld probe is developed for *in vivo* skin imaging. As for the degradation rate measurement, a semi-automatic image segmentation algorithm is designed based on U-Net to segment the collagen sponge layer of the scaffold from OCT images.

Results. The results show that the scaffold-tissue fit can be clearly visualized under OCT imaging. The degradation

Abbreviations: ADS, Artificial dermal scaffold; OCT, optical coherence tomography; CSL, collagen sponge layer; SFL, silicon film layer.

[*]Equally contributing authors.

1

is computed based on the volume of the segmented collagen sponge layer. It is observed that the ADS appears to degrade linearly with the time and in addition the degradation rate varies among different skin parts.

Conclusion. Overall, it can be concluded that OCT has a good potential to monitor the ADS *in vivo*. This can help guide the clinicians to control the treatment with the scaffold to improve the therapy.

KEYWORDS

optical coherence tomography, artificial dermal scaffold, degradation measurement, image segmentation

1 | INTRODUCTION

Skin is the largest organ of human body, which protects the underlying muscles, bones, ligaments, and organs. Serious skin damage can cause skin scar, dehydration, fatal infection, and death [1]. Skin loss is one of the common skin damages and to date, can be treated with surgical grafting methods, i.e., skin grafts [2, 3] and flaps [4, 5]. For example, skin grafts can be used for treating traumatic wounds, defects after oncologic resection, congenital skin deficiencies, vitiligo and so on. Flaps are used preferentially for the wound with deep depth and bone exposed [6]. However, although these living grafting methods contribute to the development of surgical grafting techniques, they still have some limitations [7]. Specifically, these two methods are not well suited for large skin wound and may take a risk of stimulating the trauma [1, 8]. The limitations above have prompted the development of tissue engineering technology for producing bioengineered equivalents-dermal scaffold, which has been applied in clinical treatment for skin wounds. Till now, dermal scaffold has been utilized for treating various skin wounds, such as full-thickness wounds [9], postoperative ulcers [10], burns contractures [11] and pressure sores [12].

Dermal scaffold can be classified into natural dermal scaffold and artificial dermal scaffold (ADS) [13]. Natural dermal scaffold is produced from allogeneic or heterologous skin by removing the epidermal and dermal while preserving the extracellular dermal matrix [14]. It shows the advantages of high survival rate, soft texture, and light scarring. However, it suffers from limited sources, high cost and high bio-risk [15, 16]. In contrast, ADS is produced from natural materials (i.e., collagen [17], elastin [18] and alginate [19]) and synthetic materials (polyethtlene glycol [20], poly(vinyl alcohol) [21] and polycaprolactone [22]). It exhibits advantages of good biocompatibility, controllable degradation, and low risk of disease infection [16, 23]. Till now, collagen-based ADS has been commercialized and widely used in clinic [23, 24, 25, 26].

In comparison to the continuous growing use of ADS, the supporting evaluation techniques are behindhand. Currently, hematoxylin-eosin staining and Masson's trichrome stains are often used to monitor the wound healing process and the neotissue [27]. However, these methods require harvesting specimens from the dermal scaffolds, which is invasive and painful [27, 28]. More importantly, they are dedicated to tissue assessment at cellular level while structure evaluation at large scale is missing. For example, the degradation of the dermal scaffold and the fit of the scaffold with the tissue are the two key structure properties to be monitored. The degradation extent of the dermal scaffold is critical for the clinicians to determine the timing of the second-stage skin transplantation

[29]. The degradation rate also plays a key role in cell adhesion, proliferation and penetration in wound recovery [30] and consequently needs to be under control [31]. As for the fit of the dermal scaffold with the tissue, there often exist air gaps between the scaffold and the tissue, which may slow down the vascularization of the scaffold and consequently needs to be eliminated [32]. Till now, the degradation extent and the scaffold-tissue fit are evaluated by visual observation of the scaffold's surface appearance, which is highly dependent on the clinician's experience and consequently subjective. Therefore, *in vivo* imaging techniques are desired to delineate the dermal scaffold to obtain an accurate measure on the degradation and the detection of air gap. Several conventional clinical imaging techniques have been used for monitoring the wound healing process based on scaffold. For example, high-resolution ultrasound has been applied to assess the structural changes deep in the wound [33]. Magnetic resonance imaging has been employed to evaluate the fit of human decellularized dermal matrix with the surrounding tissues [34]. However, these two imaging techniques cannot differentiate the microstructural changes due to the limited resolution [35]. In 2016, Fox et al proposed to incorporate fluorescent nanodiamond into the scaffold, allowing for assessing the scaffold degradation by fluorescence imaging [36]. However, it is invasive due to the use of imaging contrast agent and incapable to detect the air gap between the scaffold and the tissue.

Optical coherence tomography (OCT) can provide three-dimensional images of weak-scattering biological tissues with a resolution at micrometers by utilizing low-coherence optical interference [37]. OCT has achieve a great success in ophthalmology in the past decades and has become a clinic routine in ophthalmology [38, 39]. Besides, dermatology is another medical field where OCT has proven its clinic utility [40, 41, 42, 43, 44]. For example, OCT has been used for the detection of non-melanoma skin cancer [45, 46, 47] and inflammatory dermatoses, i.e., psoriasis and eczema [48]. In particular for skin wound, OCT has been developed to assess the wound depth [49], wound healing [50], and detect subcutaneous parasites [51]. As for the inspection of the dermal scaffold, OCT has only been used to look into the structure of the collagen scaffold applied on animal model [35]. To the best of our knowledge, OCT has not yet been employed to monitor the wound healing process with ADS *in vivo* and measure its degradation on human skins.

In this work, we propose to utilize OCT to monitor the degradation of the ADS and the scaffold-tissue fit. A clinic OCT prototype with a handheld probe is developed for *in vivo* skin imaging and a semi-automatic segmentation algorithm is designed based on U-Net to segment the ADS for quantitative analysis. Our method is evaluated on three patients treated with ADS. Good quality three-dimensional images of dermal scaffold can be acquired for determining its degradation. The results demonstrate the great potential of OCT for *in vivo* monitoring of the wound treatment with ADS.

2 | METHODS

2.1 | Patients

A total of three patients were recruited at the department of burn and plastic surgery of the First Affiliated Hospital of Soochow University, including two males and one female, who are 23 to 64 years old as described in Table 1. The wounds are located at ankle, head, and instep, exhibiting a size of 1.5 cm×1.2 cm to 10 cm×8 cm. All the wounds are treated with artificial dermal scaffold (BAS-1208, Lando, CN). The study was approved by the Human Research Ethics Committee of the First Affiliated Hospital of SooChow University (Suzhou, China), and the research was conducted with the principles embodied in the Declaration of Helsinki and in accordance with local statutory requirements.

TABLE 1 Patient information.

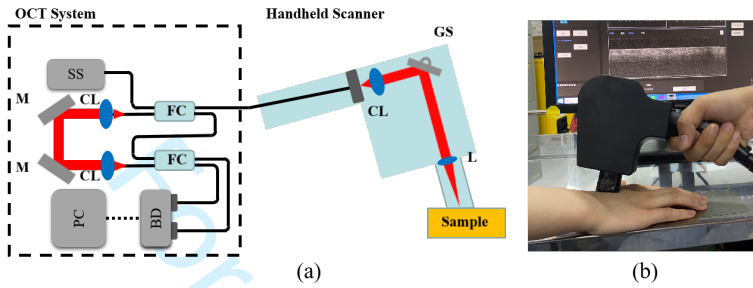| Patient	Age	Gender	Wound Area
1	58	male	ankle
2	23	female	head
3	64	male	instep

FIGURE 1 (a) Schematic of the clinical OCT system, (b) Photograph of the handheld OCT probe. SS: swept source; FC: fiber coupler; CL: collimator; M: mirror; BD: balanced photodetector; GS: galvo scanner; L: lens; PC: personal computer.

2.2 | OCT prototype system

A clinical OCT system with a handheld probe was developed for *in vivo* OCT imaging on human skin as depicted in Figure 1(a). The OCT system was designed based Michelson interferometer and built based on a wavelength-swept light source. The light source's output (SS-OCT1060, Axsun Technology, US) sweeps from about 1000 to 1100 nm at a rate of 100 kHz. The sample arm consists of a collimator (F280APC-1064, Thorlabs, US), a pair of galvo-scanners (GVSM002/M, Thorlabs, US), and a focusing lens (AC254-060-B, Thorlabs, US), which are built into a compact case to create a handheld probe. The probe tip is armed with an imaging window (WG10530-B, Thorlabs, US) titled at an angle of 10 degree to reduce the specular reflection on skin surface. The reference arm is built based on one-way light path with a pair of collimators (F240APC-1064, Thorlabs, US). The reference signal and the sample signal are combined with a 50/50 fiber coupler and eventually fed into a balanced detector (PDB471C, Thorlabs, US). The balanced detector's output passes through a low-pass filter (SLP-150+, Mini-circuits, US) to block the signal with a frequency higher than 155 MHz and then are recorded in a computer via a 12-bit dual-channel data acquisition card (ATS9351, Alazartech, US). The light beam scanning is realized by using a pair of galvo-scanners driven by a 16-bit high-speed analog output device (PCIE-6363, National Instruments, US). The axial resolution and lateral resolution of the OCT system are about 10.7 µm (in air) and 20 µm, respectively, and the imaging depth in air is about 3.78 mm. A clinic-friendly software was developed with a user-interface to show B-scan in real time.

2.3 | Imaging protocol

OCT imaging was carried out on each patient from the application of the ADS to the second-stage skin transplantation until the complete uptake of the scaffold. Three to seven OCT scans were acquired from different parts of the wound depending on the wound size upon the patients' visit to the clinicians. Each OCT imaging (C-scan) covers a field of
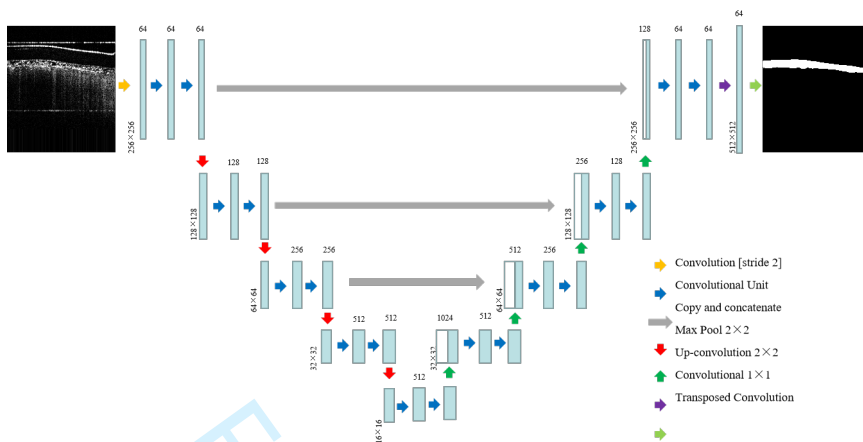
FIGURE 2   Neural Network architecture of the U-net network model. Light blue box refers to a 3D tensor. The number on top of each box denotes the number of channels (the number of filters). The number at the lower left side of the box provide the x-y-size. White boxes in the decoder part represent the concatenated tensor correspondents in the encoder part. The arrows denote the different operations.

2.8 mm×2.8 mm (512x512 pixels). The corresponding A-scan consists of 672 pixels. With an A-scan rate of 100 kHz, each C-scan takes about 3 seconds.

2.4 | Dermal scaffold degradation quantification

The ADS is constructed with silicon film layer (SFL) seated on top of collagen sponge layer (CSL). The degradation usually refers to the uptake of the CSL. Thus, the degradation rate is included in the specification of the dermal scaffold by the manufacturer and is usually determined by weighing the scaffold [1]. Apparently, the weighing method is not suitable for determining the degradation rate *in vivo* in clinical practice. Hence, in this study, we use the volume instead of the weight as the basis for calculating the degradation rate. The volume can be measured based on the 3D image of the scaffold produced by OCT. The degradation rate ($V_{DR}\%$) of the dermal scaffold was calculated by using the formula: $V_{DR}\% = (V_0-V_1)/V_0 \times 100$ (%) where V_0 and V_1 denote the volume of undegraded and degraded dermal scaffolds, respectively.

2.5 | Dermal scaffold segmentation

To determine the scaffold's degradation rate based on the volume as discussed above, the CSL of the dermal scaffold needs to be segmented from the OCT image. Hence, a semi-automatic segmentation algorithm is designed based on U-Net network for extracting the CSL from OCT images. The segmentation can be divided into two steps as the following.

First, a U-Net network model is built for segmentation as shown in Figure 2. The segmentation is implemented on B-scans as U-Net has been well demonstrated in two-dimensional medical image segmentation [52, 53]. The segmented B-scans are fused to form a three-dimensional image of the dermal scaffold. In total, there are 30 3D image datasets, of which each consists of 512 B-scans. Eighteen B-scans from each 3D image which are evenly
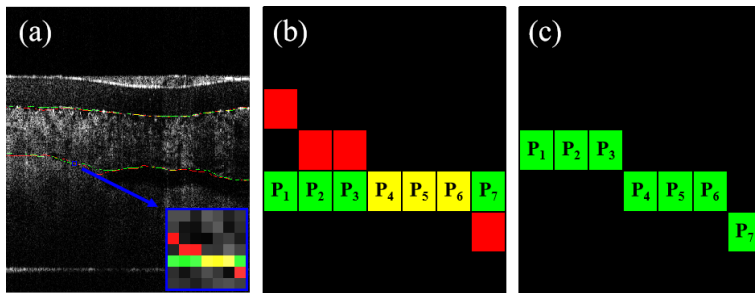
FIGURE 3 (a) B-scan of a dermal scaffold, (b) Zoomed-in image from Figure 3(a), (c) New boundary yielded by the fitting process. In Figure 3(a), red and green lines represent the boundaries of the CSL obtained by U-Net segmentation and of the reference image, respectively, and yellow lines delineate the overlap between the red and green lines.

distributed along C-scan are chosen for training and testing the segmentation model. Consequently, there are totally 540 images, of which 70% (378 images) were selected for training and the remaining 30% (162 images) were for testing.

Next, a boundary fitting algorithm is implemented to improve the segmentation to increase the measurement accuracy of the dermal scaffold's volume. This fitting algorithm is developed with an assumption that the scaffold structure shows a rigorous continuity and the dermal scaffold's boundary alters by less than one pixel between consecutive B-scans. The fitting process works as following: (1) the CSL of the dermal scaffold in the first B-scan of a 3D OCT image is annotated manually as the starting reference image; (2) the CSL's boundary in the neighboring B-scan is compared to that in the reference image. If the boundary is N pixels (N>1) away from the reference, it will be pulled towards the reference by N-1 pixels as illustrated in Figure 3. Otherwise, the boundary will remain unchanged. For example, pixel P1 is pulled downwards the green pixel by one pixel while pixels P2 to P7 remain stationary; (3) the newly adjusted boundary is set as the reference for next B-scan; (4) the second and third procedures above are repeated until all the B-scans are adjusted.

3 | RESULTS

In this study, we investigated the feasibility of using OCT to monitor artificial dermal scaffold longitudinally from two aspects: the fit of the dermal scaffold with the natural skin tissue and the degradation of the artificial dermal scaffold.

3.1 | Dermal scaffold fit

OCT imaging can provide a good insight into the structure of the dermal scaffold as illustrated in Figure 4. It is clearly seen that the dermal scaffold consists of two layers which are SFL on the top and CSL on the bottom. The SFL appears to be transparent which can be attributed to the low scattering capability. In comparison, the CSL shows a higher intensity and a sponge-like structure which is significantly different from the underlying skin. This allows for discriminating the CSL from the skin, paving the way for identifying the air gap between the CSL and the skin. Figure 4(b) describes an example of a loose fit of CSL with the underlying skin tissue. The CSL is largely detached from the skin.
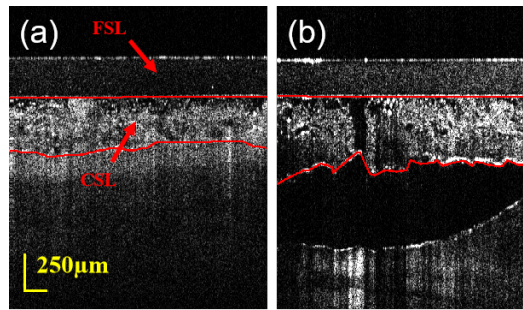
FIGURE 4   B-scan of a dermal scaffold: (a) Good scaffold-tissue fit and (b) Poor scaffold-tissue fit. The red curve delineates the upper and lower boundaries of the CSL.

3.2 | Degradation of dermal scaffolds

OCT can determine the degradation of the dermal scaffold by quantifying the CSL's volume alteration since the CSL can be clearly imaged by OCT. Figure 5(a) shows a wound covered with a ADS which is due to skin ulcer on the ankle associated with diabetes. The wound underwent OCT imaging at 2-days, 6-days, and 9-days after applying the dermal scaffold. Figures 5(b)-(d) give an example of the B-scans for those three time slots, respectively. It is seen that the CSL delineated with red boundaries exhibits a clear trend of thinning associated with the degradation process while the SFL does not show any significant thickness change. Figure 5(e) depicts the cross-sectional image of the dermal scaffold at 5-days after the second-stage free skin transplantation which was done two weeks after the dermal scaffold was applied to the wound. The second-stage free skin transplantation replaced the SFL with a free skin. As a result, there is no transparent layer on top of the CSL and instead is a bright scattering layer which is the free skin. Moreover, the CSL becomes much thinner as compared to that before the second transplantation, indicating a continuous degradation. In addition, it is also observed that the CSL's up boundary appears to be wrinkled due to the compression by the free skin as compared to the image before the second transplantation.

Besides, more morphological alterations can be found in the en-face images (Figures 5(f)-(i)). At the early stage of the dermal scaffold application, the en-face image exhibits a uniform scattering structure at the depth near the SFL layer (Figure 5(f)). In comparison, the structure tends to lose its uniformity over time as shown in Figures 5(g)-(h). Both the amount of the holes and the hole's size increase from Figure 5(f) to Figure 5(h). As for Figure 5(i), the CSL is referred to as the dark area while the bright area represents the skin tissue, implying a nearly complete degradation.

To measure the CSL's volume for determining the degradation, the CLS segmentation is required. Four prevailing deep learning networks, including U-Net [54], U-Net++ [55], Attention U-Net [56] and CS-Net [57], are evaluated in the CSL segmentation. The segmentation is evaluated with five metrics, including Pre, Recall, IoU, Dice, and F-score [58] which are summarized in Table 2. It is clearly seen that overall, U-Net performed the best among those four networks with the highest Recall (0.7474), IoU (0.6537), Dice (0.7762) and F-score (0.8112). Consequently, the following process and analysis are conducted based on the CLS images segmented with U-Net. To reduce the impact of the segmentation on the CSL volume measurement, a boundary fitting algorithm is developed to correct those segmentation errors by utilizing the structural continuity between consecutive B-scans. It is found that the Pre, Recall, IoU, Dice and F-score are increased by the fitting algorithm from 0.8871, 0.7474, 0.6537, 0.7762, and 0.8112 to 0.8882, 0.9036, 0.8032, 0.8873, and 0.8958, respectively.
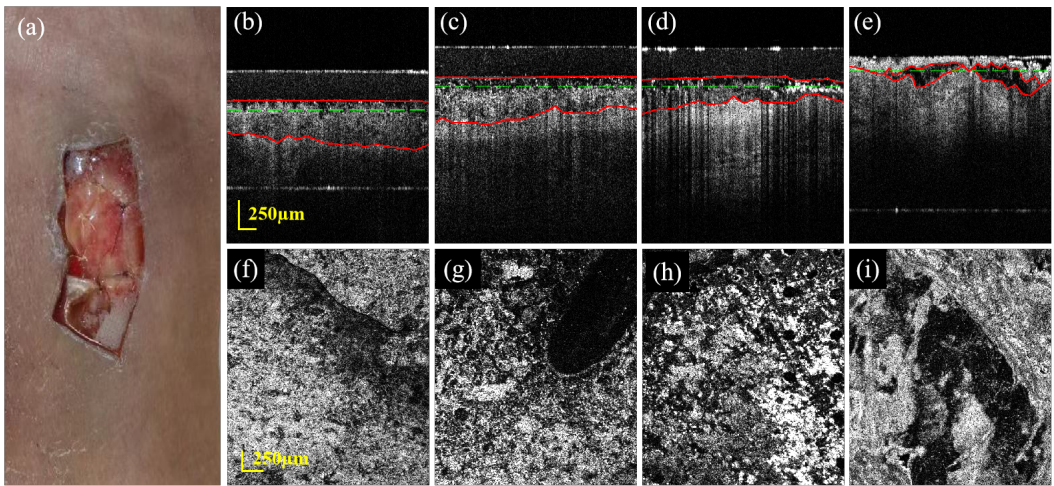
FIGURE 5 (a) Photo of patient's wound covered with a ADS, (b)-(d) B-scan of the ADS at 2-days, 6-days, 9-days after dermal scaffold coverage, respectively, (e) B-scan of the ADS at 19-days after dermal scaffold coverage and 5 days after second-stage skin transplantation, (f)-(i) are the en-face images of the CSL corresponding to (b)-(e). The green dashed line in (b)-(e) indicates the depth of the en-face image, and the red curve is the upper and lower boundaries of the CSL.

TABLE 2 CSL segmentation results.

Methods	Pre	Recall	IoU	Dice	F-score
U-Net	0.8871	**0.7474**	**0.6537**	**0.7762**	**0.8112**
U-Net++	0.9308	0.6903	0.6455	0.7666	0.7927
Attention U-Net	0.8920	0.6919	0.6194	0.7466	0.7793
CS-Net	**0.9524**	0.6107	0.5902	0.7165	0.7442

Figures 6(a)-(d) show the segmented 3D images of the CSL corresponding to Figures 5(b)-(e), respectively. Based on the 3D images, the thickness maps are computed as illustrated in Figures 6(e)-(h). The thickness seems not to be uniform and as seen in Figure 6(a), the thickness varies a lot laterally. However, a clear thinning trend can be found over time. In addition, after the second-stage free skin transplantation (Figure 6(d)), the CSL shows a big loss.

Next, the segmented CSL image is binarized with the noise floor as the threshold. The noise floor is determined by averaging the intensity over the holes in the CSL image. With the binary image, the CSL volume is measured by counting all the non-zero pixels. Figure 7 depicts the CSL degradation of three patients as a function of time. For each degradation calculation, the volumes of two to three good-quality 3D images are averaged, which are acquired at various positions of the same wound. It needs to be pointed out that two 3D images were excluded due to their significantly larger CSL volumes as compared to other 3D images measured on the same day. For one 3D image, the large CSL volume is probably due to the large detachment of ADS from the underlying tissue. This detachment can prevent protease from infiltrating the scaffold and consequently slow down the CSL degradation. For the other 3D image, it may be explained by the segmentation error due to the weak distinction between the CSL and the tissue.

For each patient, the first 3D image is used as the base (undegraded) for the degradation calculation and conse-
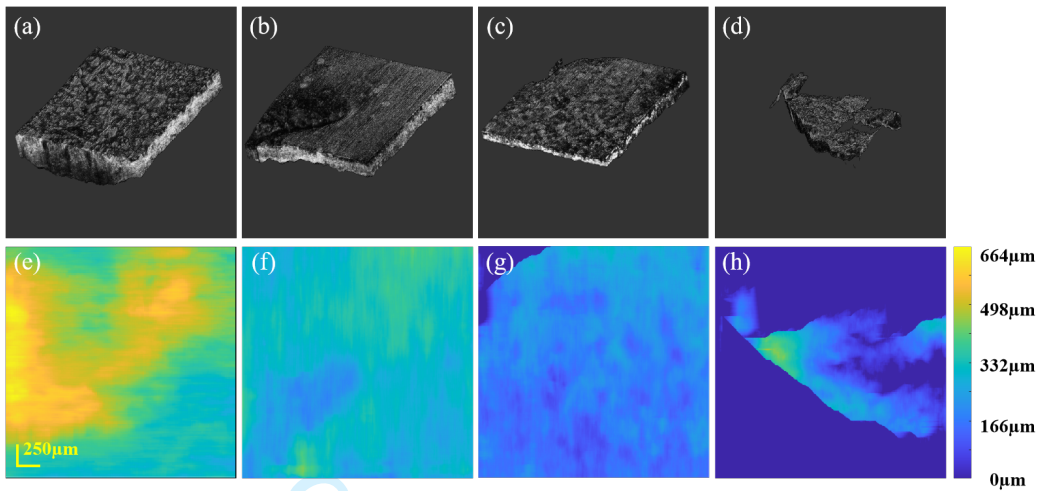
FIGURE 6 (a)-(d) Three-dimensional images of the segmented CSL corresponding to Figures 5(b)-(e), respectively. (e)-(h) Thickness maps measured from Figures 6(a)-(d), respectively.

quently the corresponding degradation is zero. Overall, similar degradation rates are observed on patients 1 and 3 while much slower degradation on patient 2. In addition, for patients 2 and 3, the dermal scaffold undergoes a slow degradation during the first nine days followed by a fast degradation. This degradation trend does not occur on patient 1. This may be because the wounds on patients 2 and 3 were treated with a negative pressure drainage system for one week after the dermal scaffold was applied. To evaluate the degradation trend quantitatively, the degradation curves were fitted with a linear function to obtain an average degradation rate. Due to the impact of the negative pressure drainage system, the starting degradation was excluded in the fitting process for patients 2 and 3 to achieve a fair comparison among all the three patients. The slopes of the linearly fitting function are 5.51, 2.66, and 4.53 percentage/day for patients 1 to 3, respectively.

4 | DISCUSSION

In this study, we demonstrated that OCT imaging is well capable to visualize the fit of the dermal scaffold with the neighboring natural tissue as illustrated in Figure 4. This can effectively help clinicians to find and locate the loose fit, and take measures, i.e., compression, to obtain a tight fit. If the loose fit is untreated, this will obscure the vascularization of the CSL. This can be accounted for by the fact that the detachment prevents the extracellular matrix secretion from impregnating the scaffold, and the fibroblasts from growing into the dermal scaffold, and results in a reduced delivery of nutrient into the dermal scaffold [59]. Furthermore, the survival rate of the free skin tissue is greatly dependent on the degree of the CSL's vascularization. Consequently, a tight dermal scaffold fit is highly desired to achieve a high survival rate of the transplanted skin [32, 60].

As for the degradation measurement, the ADS underwent a degradation at a similar speed for patient 1 and 3. This may be explained by the fact that both wounds are on the ankle. In addition, these two patients show the same sex and a similar age. In comparison, the degradation speed is reduced nearly by a fact of two for the dermal scaffold applied to the head. These findings imply that the degradation rate is likely to be dependent on the would location
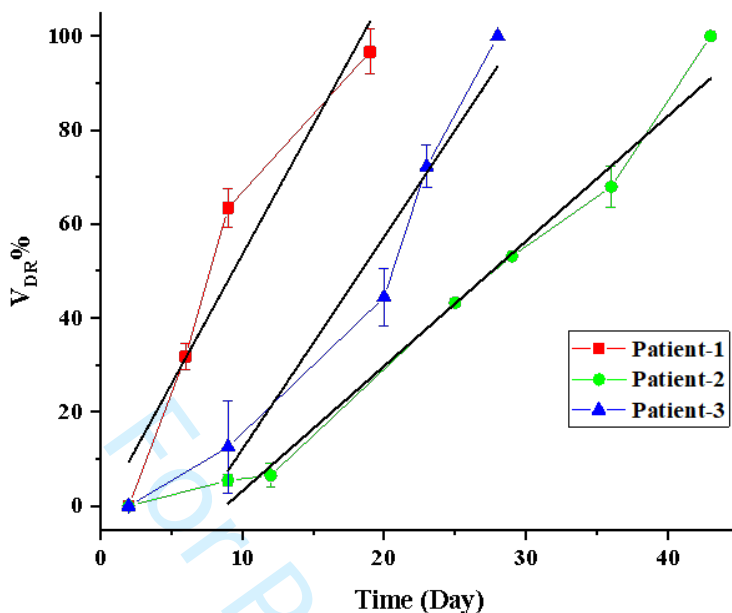
FIGURE 7 The degradation rate of the CSL as a function time. The black line represents the linear fitting of the degradation function.

and a consistent degradation rate can be expected for the same skin location. However, a larger dataset is needed to further verify it.

Finally, it is worthy to take out patient 3's last OCT imaging for analysis which was conducted at 13 days after the second-stage skin transplantation. The wound is a skin ulcer caused by scalding as shown in Figure 8(a). The patient recovered well after skin transplantation and did not suffer any inflammation. In B-scan (Figure 8(b)), it seems that there is no CSL left inside the tissue, indicating that a complete degradation has occurred. The degradation at 5 days earlier was measured to be about 70%. According to the degradation function, this complete degradation should be close to the last OCT measurement. Moreover, this dermal scaffold treatment was assessed by comparing with the surrounding healthy tissue. In the B-scans of the treated tissue and healthy tissue (Figures 8(b)-(c)), it is seen that the blood vessels start to be present around the depth denoted with green dashed line and more large vessels are observed in the healthy tissue, which are more obvious in the corresponding en-face images (Figures 8(d)-(e)). This suggests that OCT angiography can further enhance the capability of OCT in evaluate the would treatment with the ADS by providing the vasculature images.

5 | CONCLUSION

In this work, OCT is proposed to monitor the artificial dermal scaffold *in vivo*. An OCT prototype with a handheld probe was developed for clinic measurement. It was demonstrated successfully that OCT imaging can provide a rapid and accurate evaluation about the fit of the dermal scaffold with the natural skin tissue. Moreover, OCT imaging was utilized for measuring the dermal scaffold's degradation rate. The degradation rate is determined based on the scaffold volume instead of the weight. Thus, a semi-automatic image segmentation model based on U-Net was designed to
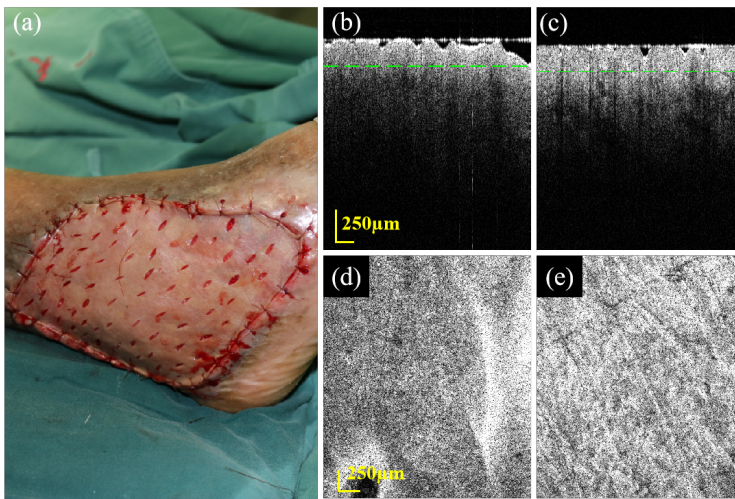
FIGURE 8 Photo of patient's wound covered with free skin, (b)-(c) B-scans of the wound at 13-days after free skin transplantation and healthy skin, respectively, (d)-(e) en-face images of the CSL corresponding to (b)-(c). The green dashed line in (b)-(c) denotes the depth of the en-face image.

segment the CSL from OCT image for the volume measurement and furthermore a boundary fitting algorithm was developed to improve the volume measurement by reducing the impact of the segmentation errors. The results show that OCT imaging has a good potential to be an effective tool for longitudinally monitoring the dermal scaffold's degradation *in vivo*. This can help clinicians to make the dermal scaffold degrade at a proper rate to obtain a good wound therapy efficacy. In the future, the method developed for measuring the degradation rate is expected to be validated on a larger dataset from various skin parts of human body and further optimized to be used as a clinic routine. In addition, OCT angiography will be integrated into the current method to provide a more extensive evaluation.

Data availability

Data underlying the results presented in this paper are not publicly available at this time but may be obtained from the authors upon reasonable request.

Conflict of interest

The authors declare no conflicts of interests.

references

[1] Wang F, Wang M, She Z, Fan K, Xu C, Chu B, et al. Collagen/chitosan based two-compartment and bi-functional dermal scaffolds for skin regeneration. Materials Science and Engineering: C 2015;52:155–162.

[2] Abdelrahman I, Steinvall I, Sjöberg F, Ellabban MA, Zdolsek J, Elmasry M. Pros and Cons of Early and Late Skin Grafting in Children with Burnsmdash;Evaluation of Common Concepts. European Burn Journal 2022;3(1).

[3] van Zuijlen PP, Van Trier AJ, Vloemans JF, Groenevelt F, Kreis RW, Middelkoop E. Graft survival and effectiveness of

dermal substitution in burns and reconstructive surgery in a one-stage grafting model. Plastic reconstructive surgery 2000;106(3):615–623.

[4] Janik S, Eljazzar R, Faisal M, Grasl S, Vyskocil E, Miles BA, et al. Outcome in Patients with Partial and Full-Thickness Cheek Defects following Free Flap Reconstruction—A Multicentric Analysis of 47 Cases. Journal of Clinical Medicine 2020;9(6).

[5] Hallock GG. The utility of both muscle and fascia flaps in severe upper extremity trauma. Journal of Trauma Acute Care Surgery 2002;53(1):61–65.

[6] Shimizu R, Kishi K. Skin graft. Plastic surgery international 2012;2012.

[7] Petkar KS, Dhanraj P, Kingsly PM, Sreekar H, Lakshmanarao A, Lamba S, et al. A prospective randomized controlled trial comparing negative pressure dressing and conventional dressing methods on split-thickness skin grafts in burned patients. Burns 2011;37(6):925–929.

[8] Sun BK, Siprashvili Z, Khavari PA. Advances in skin grafting and treatment of cutaneous wounds. Science 2014;346(6212):941–945.

[9] Mirzaei-parsa MJ, Ghanbari H, Alipoor B, Tavakoli A, Najafabadi MRH, Faridi-Majidi R. Nanofiber-acellular dermal matrix as a bilayer scaffold containing mesenchymal stem cell for healing of full-thickness skin wounds. Cell and Tissue Research 2019;375(3):709–721.

[10] Niimi Y, Baba K, Tsuchida M, Takeda A. A Histological Evaluation of Artificial Dermal Scaffold Used in Micrograft Treatment: A Case Study of Micrograft and NPWT Performed on a Postoperative Ulcer Formation after Tumor Resection. Medicina 2022;58(1):73.

[11] Parcells AL, Karcich J, Granick MS, Marano MA. The Use of Fetal Bovine Dermal Scaffold (PriMatrix) in the Management of Full-Thickness Hand Burns. Eplasty 2014;14:e36.

[12] Sharma V, Kohli N, Moulding D, Afolabi H, Hook L, Mason C, et al. Design of a Novel Two-Component Hybrid Dermal Scaffold for the Treatment of Pressure Sores. Macromolecular Bioscience 2017;17(11):1700185.

[13] Zhou H, You C, Wang X, Jin R, Wu P, Li Q, et al. The progress and challenges for dermal regeneration in tissue engineering. Journal of Biomedical Materials Research Part A 2017;105(4):1208–1218.

[14] Tavelli L, Barootchi S, Di Gianfilippo R, Modarressi M, Cairo F, Rasperini G, et al. Acellular dermal matrix and coronally advanced flap or tunnel technique in the treatment of multiple adjacent gingival recessions. A 12-year follow-up from a randomized clinical trial. Journal of Clinical Periodontology 2019;46(9):937–948.

[15] Xu Z, Chen X, Tan R, She Z, Chen Z, Xia Z. Preparation and characterization of a gallium-loaded antimicrobial artificial dermal scaffold. Materials Science and Engineering: C 2019;105:110063.

[16] Zhang Q, Chen S, You R, Tariq Z, Huang J, Li M, et al. Silk fibroin/hyaluronic acid porous scaffold for dermal wound healing. Fibers and Polymers 2017;18(6):1056–1063.

[17] Heimbach DM, Warden GD, Luterman A, Jordan MH, Ozobia N, Ryan CM, et al. Multicenter postapproval clinical trial of Integra® dermal regeneration template for burn treatment. The Journal of burn care rehabilitatio 2003;24(1):42–48.

[18] Rnjak-Kovacina J, Wise SG, Li Z, Maitz PK, Young CJ, Wang Y, et al. Electrospun synthetic human elastin: collagen composite scaffolds for dermal tissue engineering. Acta biomaterialia 2012;8(10):3714–3722.

[19] Chandika P, Ko SC, Oh GW, Heo SY, Nguyen VT, Jeon YJ, et al. Fish collagen/alginate/chitooligosaccharides integrated scaffold for skin tissue regeneration application. International journal of biological macromolecules 2015;81:504–513.

[20] Vahidi M, Frounchi M, Dadbin S. Porous gelatin/poly (ethylene glycol) scaffolds for skin cells. Soft Materials 2017;15(1):95–102.

[21] Asran AS, Razghandi K, Aggarwal N, Michler GH, Groth T. Nanofibers from blends of polyvinyl alcohol and polyhydroxy butyrate as potential scaffold material for tissue engineering of skin. Biomacromolecules 2010;11(12):3413–3421.

[22] Bonvallet PP, Culpepper BK, Bain JL, Schultz MJ, Thomas SJ, Bellis SL. Microporous dermal-like electrospun scaffolds promote accelerated skin regeneration. Tissue Engineering Part A 2014;20(17-18):2434–2445.

[23] Matsumoto Y, Ikeda K, Yamaya Y, Yamashita K, Saito T, Hoshino Y, et al. The usefulness of the collagen and elastin sponge derived from salmon as an artificial dermis and scaffold for tissue engineerin. Biomedical Research 2011;32(1):29–36.

[24] Li J, Ren N, Qiu J, Jiang H, Zhao H, Wang G, et al. Carbodiimide crosslinked collagen from porcine dermal matrix for high-strength tissue engineering scaffold. International Journal of Biological Macromolecules 2013;61:69–74.

[25] Brown SJ, Surti F, Sibbons P, Hook L. Wound healing properties of a fibrin-based dermal replacement scaffold. Biomedical Physics Engineering Express 2021;8(1):015025.

[26] Huang S, Deng T, Wang Y, Deng Z, He L, Liu S, et al. Multifunctional implantable particles for skin tissue regeneration: preparation, characterization, in vitro and in vivo studies. Acta Biomaterialia 2008;4(4):1057–1066.

[27] Yan S, Zhang Q, Wang J, Liu Y, Lu S, Li M, et al. Silk fibroin/chondroitin sulfate/hyaluronic acid ternary scaffolds for dermal tissue reconstruction. Acta Biomaterialia 2013;9(6):6771–6782.

[28] Ojeh N, Frame J, Navsaria H. In vitro characterization of an artificial dermal scaffold. Tissue engineering 2001;7(4):457–472.

[29] Zomer HD, da Silva Jeremias T, Ratner B, Trentin AG. Mesenchymal stromal cells from dermal and adipose tissues induce macrophage polarization to a pro-repair phenotype and improve skin wound healing. Cytotherapy 2020;22(5):247–260.

[30] Sharma V, Patel N, Kohli N, Ravindran N, Hook L, Mason C, et al. Viscoelastic, physical, and bio-degradable properties of dermal scaffolds and related cell behaviour. Biomedical Materials 2016;11(5):055001.

[31] Chawla R, Tan A, Ahmed M, Crowley C, Moiemen NS, Cui Z, et al. A polyhedral oligomeric silsesquioxane–based bilayered dermal scaffold seeded with adipose tissue–derived stem cells: in vitro assessment of biomechanical properties. Journal of Surgical Research 2014;188(2):361–372.

[32] Agostinis C, Spazzapan M, Vuerich R, Balduit A, Stocco C, Mangogna A, et al. Differential Capability of Clinically Employed Dermal Regeneration Scaffolds to Support Vascularization for Tissue Bioengineering. Biomedicines 2021;9(10).

[33] Kuhn C, Angehrn F. Use of high-resolution ultrasound to monitor the healing of leg ulcers: a prospective single-center study. Skin Research Technology 2009;15(2):161–167.

[34] Ghettia M, Bondioli E, Purpura V, Cenacchi G, Ruscelli P, Melandri D. Decellularized human dermal matrix produced by a skin bank. Ann Ital Chir 2017;88(5):443–448.

[35] Wang Z, Pan H, Yuan Z, Liu J, Chen W, Pan Y. Assessment of Dermal Wound Repair after Collagen Implantation with Optical Coherence Tomography. Tissue Engineering Part C: Methods 2008;14(1):35–45.

[36] Fox K, Tran PA, Lau DW, Ohshima T, Greentree AD, Gibson BC. Nanodiamond-polycaprolactone composite: A new material for tissue engineering with sub-dermal imaging capabilities. Materials Letters 2016;185:185–188.

[37] Münter M, Vom Endt M, Pieper M, Casper M, Ahrens M, Kohlfaerber T, et al. Dynamic contrast in scanning microscopic OCT. Optics Letters 2020;45(17):4766–4769.

[38] Fercher A, Mengedoht K, Werner W. Eye-length measurement by interferometry with partially coherent light. Optics letters 1988;13(3):186–188.

[39] Wang Y, Liu S, Lou S, Zhang W, Cai H, Chen X. Application of optical coherence tomography in clinical diagnosis. Journal of X-ray Science and Technology 2019;27(6):995–1006.

[40] Sattler EC, Kästle R, Welzel J. Optical coherence tomography in dermatology. Journal of biomedical optics 2013;18(6):061224.

[41] Pierce MC, Strasswimmer J, Park BH, Cense B, De Boer JF. Advances in optical coherence tomography imaging for dermatology. Journal of investigative dermatology 2004;123(3):458–463.

[42] Gong P, Es'haghian S, Harms KA, Murray A, Rea S, Kennedy BF, et al. Optical coherence tomography for longitudinal monitoring of vasculature in scars treated with laser fractionation. Journal of Biophotonics 2016;9(6):626–636.

[43] Yow AP, Cheng J, Li A, Srivastava R, Liu J, Wong DWK, et al. Automated in vivo 3D high-definition optical coherence tomography skin analysis system. In: 2016 38th Annual International Conference of the IEEE Engineering in Medicine and Biology Society (EMBC);. p. 3895–3898.

[44] Welzel J, Lankenau E, Birngruber R, Engelhardt R. Optical coherence tomography of the human skin. Journal of the American Academy of Dermatology 1997;37(6):958–963.

[45] Duan L, Marvdashti T, Lee A, Tang JY, Ellerbee AK. Automated identification of basal cell carcinoma by polarization-sensitive optical coherence tomography. Biomedical optics express 2014;5(10):3717–3729.

[46] Maier T, Kulichová D, Ruzicka T, Kunte C, Berking C. Ex vivo high-definition optical coherence tomography of basal cell carcinoma compared to frozen-section histology in micrographic surgery: a pilot study. Journal of the European Academy of Dermatology Venereology 2014;28(1):80–85.

[47] Hinz T, Ehler LK, Hornung T, Voth H, Fortmeier I, Maier T, et al. Preoperative characterization of basal cell carcinoma comparing tumour thickness measurement by optical coherence tomography, 20-MHz ultrasound and histopathology. Acta dermato-venereologica 2012;92(2):132–137.

[48] Wan B, Ganier C, Du-Harpur X, Harun N, Watt F, Patalay R, et al. Applications and future directions for optical coherence tomography in dermatology. British Journal of Dermatology 2021;184(6):1014–1022.

[49] Saxer CE, de Boer JF, Park BH, Zhao Y, Chen Z, Nelson JS. High-speed fiber–based polarization-sensitive optical coherence tomography of in vivo human skin. Optics letters 2000;25(18):1355–1357.

[50] Cobb MJ, Chen Y, Underwood RA, Usui ML, Olerud J, Li X. Noninvasive assessment of cutaneous wound healing using ultrahigh-resolution optical coherence tomography. Journal of biomedical optics 2006;11(6):064002.

[51] Maier T, Sattler E, Braun-Falco M, Ruzicka T, Berking C. High-definition optical coherence tomography for the in vivo detection of demodex mites. Dermatology 2012;225(3):271–276.

[52] Kugelman J, Alonso-Caneiro D, Read SA, Hamwood J, Vincent SJ, Chen FK, et al. Automatic choroidal segmentation in OCT images using supervised deep learning methods. Scientific Reports 2019;9(1):13298.

[53] Dos Santos VA, Schmetterer L, Stegmann H, Pfister M, Messner A, Schmidinger G, et al. CorneaNet: fast segmentation of cornea OCT scans of healthy and keratoconic eyes using deep learning. Biomedical optics express 2019;10(2):622–641.

[54] Ronneberger O, Fischer P, Brox T. U-Net: Convolutional Networks for Biomedical Image Segmentation. Springer International Publishing 2015;.

[55] Zhou Z, Siddiquee M, Tajbakhsh N, Liang J. UNet++: Redesigning Skip Connections to Exploit Multiscale Features in Image Segmentation. IEEE Transactions on Medical Imaging 2020;39(6):1856–1867.

[56] Oktay O, Schlemper J, Folgoc LL, Lee M, Heinrich M, Misawa K, et al. Attention U-Net: Learning Where to Look for the Pancreas. arXiv preprint 2018;.

[57] Mou L, Zhao Y, Chen L, Cheng J, Liu J. CS-Net: Channel and Spatial Attention Network for Curvilinear Structure Segmentation. Medical Image Computing and Computer Assisted Intervention – MICCAI 2019, 22nd International Conference, Shenzhen, China, October 13–17, 2019, Proceedings, Part I; 2019.

[58] Yang C, Zhou X, Zhu W, Xiang D, Chen Z, Yuan J, et al. Multi-Discriminator Adversarial Convolutional Network for Nerve Fiber Segmentation in Confocal Corneal Microscopy Images. IEEE Journal of Biomedical and Health Informatics 2022;26(2):648–659.

[59] Qiu X, Wang J, Wang G, Wen H. Vascularization of Lando® dermal scaffold in an acute full-thickness skin-defect porcine model. Journal of Plastic Surgery Hand Surgery 2018;52(4):204–209.

[60] Wang W, Yu Y, Jiang Y, Qu J, Niu L, Yang J, et al. Silk fibroin scaffolds loaded with angiogenic genes in adenovirus vectors for tissue regeneration. Journal of Tissue Engineering and Regenerative Medicine 2019;13(5):715–728.